
Paper:
Hardcastle, TP, Seabourne, CR, Brydson, RMD, Livi, KJT and Scott, AJ (2013) *The energy of step defects on the TiO2 rutile (110) surface: An ab initio DFT methodology.* Journal of Physical Chemistry Part C: Nanomaterials and Interfaces, 117 (45). 23766 - 23780.

http://dx.doi.org/10.1021/jp4078135

The energy of step defects on the TiO_2 rutile (110) surface: An ab initio DFT methodology

Trevor P. Hardcastle,[§] *Che R. Seabourne,*[§] *Rik M. D. Brydson,*[§] *Ken J. T. Livi,*[‡] *and*

Andrew J. Scott.[*§]

[§]Institute for Materials Research, SPEME, University of Leeds, Leeds LS2 9JT, UK

[‡]Johns Hopkins University, Baltimore, MD 21218, USA

ABSTRACT: We present a novel methodology for dealing with quantum size effects (QSE) when calculating the energy per unit length and step-step interaction energy of atomic step defects on crystalline solid surfaces using atomistic slab models. We apply it to the TiO_2 rutile (110) surface using density functional theory (DFT) for which it is well known that surface energies converge in a slow and oscillatory manner with increasing slab size. This makes it difficult to reliably calculate step energies because they are very sensitive to supercell surface energies, and yet the surface energies depend sensitively on the choice of slab chemical formula due to the dominance of QSE at computationally practical slab sizes. The commonly used method of calculating surface energies by taking the intercept of a best fit line of total supercell energies against slab size breaks down and becomes highly unreliable for such systems. Our systematic approach, which can be applied to any crystalline surface, bypasses such statistical estimation techniques and cross-checks and makes robust what is otherwise a very unreliable process of extracting the energies of steps. We use the calculated step energies to predict island shapes on rutile (110) which compare favourably with published scanning tunneling microscopy (STM) images.

Keywords: vicinal, metal oxide, characterization, STM, density functional theory, island

1. INTRODUCTION

1.1. The importance of steps on TiO_2

The surface science of TiO_2 is of persistent and widespread interest in materials science because of the many industrial applications which exploit its properties as a photocatalyst[1], including bactericidal coatings[2-4], air and water purification[5,6] and photo-induced superhydrophilic surfaces.[7-9] Alongside technological motivations, TiO_2 surfaces are of interest in the geosciences because step defects are thought to act as bonding sites for organic molecules in aqueous solutions providing a possible basis for the origins of primordial life.[10-15] The (110) surface of the rutile phase is particularly important because rutile is the most abundant macroscopic phase of TiO_2 and the (110) surface is the most stable surface of this phase,[16,17] comprising the majority of the total surface area in laboratory samples. Scanning tunnelling microscopy (STM) studies[18-22] have emerged since the early 1990's which invariably show that extended step defects comprise a very significant proportion of the overall surface area of rutile (110). Thus, a proper understanding of steps on the atomic level is crucial in moving towards a complete characterisation of this extremely important system, which has in many ways become the archetypal representative for transition metal oxide surfaces. The surface of metal oxides is where many of the physical and chemical processes of interest to existing and emerging technologies takes place, and the specific atomic configurations of step structures can have a very significant effect on the surface chemistry of metal oxides and their affinity for bonding with adsorbates.[16] This is especially true for crystalline nanoparticles on which steps are likely to dominate the surface morphology. Theoretical studies of the energy and structure of steps therefore present opportunities to not only optimise existing metal oxide surface processes but also to predict surface-adsorbate bonding processes to be exploited for new technologies.

1.2. Existing studies of steps on TiO_2

In published STM studies[18-22] of vacuum-annealed rutile (110) surfaces, terraces bound by extended step defects running almost exclusively along the $\langle 1\bar{1}1 \rangle$ and $\langle 001 \rangle$ directions are observable, where the surface roughness is seen to decrease with higher annealing temperatures. Among these studies, Onishi et al.[19] was the first to discover a new surface phase of highly organised "double-strand rows" after annealing at 1150 K, although we don't consider that phase here. These studies have also shown that the vacuum-annealing preparation process for rutile (110) samples creates a small concentration of O vacancies and so these samples are slightly substoichiometric in O. In this work, we focus on the case of stoichiometric models in common with conventional surface energy calculations. This is because attempts to calculate surface energies for non-stoichiometric selections of binary compounds immediately result in an *a priori* conflict with the definition of surface energy itself. A detailed discussion of O substoichiometry on rutile (110) samples is given in section 3.6. Despite these STM studies showing that steps are clearly extended along well-defined crystallographic directions, the exact atomic arrangement along the steps is difficult to determine theoretically with certainty. The difficulty is that the annealing or cleaving process may provide the energetic perturbations required for surface atoms to overcome local reconstruction activation barriers and relax into a configuration which cannot be obtained by cleaving the bulk structure. However, Martinez et al.[23] recently harnessed the predictive power of a genetic algorithm with density functional theory (DFT) to tackle this difficulty for $\langle 1\bar{1}1\rangle$ and $\langle 001\rangle$ type steps on rutile (110). By sampling a large number of candidate step structures on a stoichiometric (451) slab, the most stable atomic arrangement which they recovered for $\langle 1\bar{1}1\rangle$ steps is found to be *not* obtainable from a bulk truncation, but is instead formed by adding an extra TiO_2 unit to the surface cell, a structure which they coined $\langle 1\bar{1}1\rangle_R$. Their study clearly demonstrates the importance of exhaustive structure searching methods in the characterisation of annealed surfaces. The most energetically stable $\langle 001\rangle$ step structures that they recovered were two stoichiometric bulk-truncated terminations, both of which are considered in this study. In their study, they calculated total supercell energies which reveal the overall stability of vicinal surfaces. However, the individual energetic components of high-index surfaces can not be extracted from such comparisons of total supercell energy.

1.3. Step energy calculations are difficult because of quantum size effects

Theoretical calculations of the properties of material surfaces using periodic slab models of computationally practical size are often strongly influenced by QSE.[24-37] For the case of TiO_2 rutile (110), Bredow et al. showed that dominant QSE exist in the form of alternating modes of Ti 3d and O 2p electronic orbital hybridisation caused by the alternating odd/even number of oxide layers in slabs of increasing thickness.[34] All ground-state material properties are derived from the electron density in DFT calculations, so Bredow's paper is significant because it is indicative of the very general and widespread issue of dealing with QSE when modelling any surface property for materials in which QSE are strong. It is well established from published DFT calculations that TiO_2 rutile surface energies[17,24-27,35-37], surface vacancy formation energies[26,28,29] and other surface energetic properties such as molecular adsorption energies[30-33] all converge in a slow and oscillatory way with increasing slab thickness. This general situation means that calculating step energies accurately using high-index surfaces using slab models is difficult. This is because the step energy is tiny compared to the surface energy, and the surface energy (itself tiny compared to total supercell energies) is very sensitive to the choice of slab structure.

There is one commonly used statistical method of estimating surface energies which has been used in the literature.[35,38-40,41], which is to plot the total energies of increasingly large slab/vacuum supercells against the number of atoms or formula units in the slab, and to then use linear regression to draw a best fit line and interpret the small positive intercept of this best fit line as the surface energy at infinite slab thickness. It is absolutely critical that this approach is *avoided* for materials in which surface energies converge in a slow and oscillatory manner with increasing slab size, such as TiO_2 rutile. For such systems, this method can give vastly different intercepts depending on which slab energy data points are chosen to be included in the fit, and therefore vastly different estimates of the surface energy. This is an unacceptable situation; the "surface energy" cannot be allowed to depend so dramatically on the arbitrary choice of which slab energies are included in the data range. If this fitting approach is used on high-index surface slabs with the intention of extracting the tiny and extremely sensitive energies of steps, it fails spectacularly, and for the same reason. In Section 1 of the Supporting Information, we elaborate further on this issue and provide a detailed discussion of why linear fitting approaches to surface energy estimation should be avoided in materials like TiO_2 rutile where surface-surface interactions are strong. Alongside this obvious practical limitation, we also argue that using a linear fitting approach in this context has some questionable underlying assumptions because it fails to properly recognize surface energy oscillations in TiO_2 rutile as a non-random, reproduceable and physically significant manifestation of alternating configurations of electron density, as already explained by Bredow et al.,[34] and instead wrongly treats them as random deviations from a linear trend characterised by a Gaussian distribution. From a practical point of view, it is worth noting that linear fitting methods work without problems for materials in which surface energies can easily be fully converged with slab thickness (such as metals) as long as the unconverged surface energies from the very thinnest slabs are not included in the fit. There are examples in the literature of robust uses of linear fitting on ledge energies[42,43] (step + interaction energy), linear fitting on high-index surface energies[44], and direct extraction of step energies from vicinal slabs[45,46], where, in all cases, it was ensured that total surface energies were fully converged at the slab thicknesses used. The difficulty with systems like TiO_2 rutile is that linear fitting techniques do not work, and neither does the "brute force" approach of using arbitrarily large slabs because of the very long-ranged nature of surface-surface interactions.

Despite the apparent hindrance of QSE to slab calculations for systems like TiO_2, the slow convergence of surface energies with slab sizes actually constitutes a rich source of data which has apparently not yet been exploited in any published articles. In this article, we demonstrate a new systematic approach to extracting the energies of steps which fully uses this data to cross-check and make robust what is otherwise a potentially unreliable method. In order that our suggested methodology be open to scrutiny and improvement, and for the sake of reproducibility, we lay out the elementary details in section 1.4. Further details are also provided in Section 2 of the Supporting Information. We then apply our methodology to the rutile (110) surface using DFT and we use the calculated step energies to predict island shapes as a function of slab thickness for comparison with published STM images showing terrace islands on this surface. The atomic configuration difficulty described above is tackled by focusing on the lowest energy step structures recently predicted by Martinez et al.[23]; specifically, the two most stable structures along the $\langle 1\bar{1}1\rangle$ direction and the two most stable structures along the $\langle 001\rangle$ direction. These four steps are illustrated in Figure 1. We adopt similar notation for the step energies as those used in 2006 for the case of steps on TiO_2 anatase (101) by Gong et al.,[40] from which we took much of our original inspiration. In their study, the authors calculated the energies of steps theoretically using supercells with DFT. However, the authors of this study used linear fitting to obtain their surface energies, and comprehensive technical details of their methodology and data analysis were not provided, so it is unclear whether they encountered any difficulties relating to QSE, and how they handled them if so.

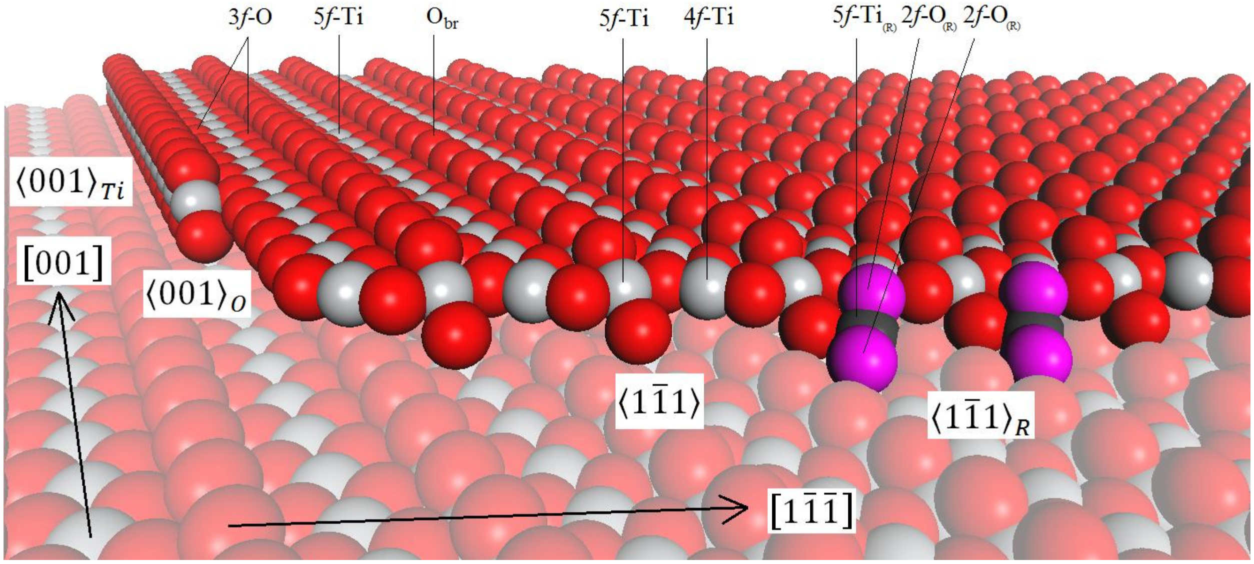

Figure 1. *The edge of a terrace island bound by* $\langle 001\rangle$*- and* $\langle 1\bar{1}1\rangle$*-direction step structures on the stoichiometric (110) surface of* TiO_2 *rutile. The structures* $\langle 001\rangle_{Ti}$, $\langle 001\rangle_{O}$, $\langle 1\bar{1}1\rangle$ *and* $\langle 1\bar{1}1\rangle_{R}$, *are the lowest energy stoichiometric structures theoretically predicted by Martinez et al.*[23] *The extra* TiO_2 *units of the* $\langle 1\bar{1}1\rangle_{R}$ *structure are depicted in purple and dark grey to signify that their positions do not correspond to frozen bulk truncations.*

1.4. Methodology

To calculate the energies of steps and their interactions, we model high-index vicinal surfaces with Miller indices (hkl) which lie at a small angle θ_{hkl} to the (110) plane. For a vicinal surface, the total surface energy per unit area (of the plane (hkl)), γ_{hkl}, can be expressed as (see Supporting Information)

$$\frac{\gamma_{hkl}}{cos\theta_{hkl}} = \gamma_{110} + \frac{\beta}{d_{hkl}} + \frac{q}{{d_{hkl}}^3}, \tag{1}$$

where γ_{110} is the surface energy per unit area of a pristine (110) terrace, β is the energy per unit length along an isolated step, q is the interaction constant representing the strength of the step-step interaction and d_{hkl} is the step-step seperation distance measured in the (110) plane. Note the important distinction between these elastic step-step interactions associated with strain, and the entirely different step-step repulsion associated with the presence of kinks due to configurational entropy at non-zero temperature.[47-49] We adopt the notation used by Gong et al.[40] for the terrace, step and step-step interaction terms for consistency. By writing the interaction term in the form q/d^3, we have provisionally adopted the $\sim 1/d^2$ interaction potential of Marchenko and Parshin[50] (MP) derived from the general surface stress tensor for continuum solids. By using stoichiometric slab/vacuum supercells, numerical values for γ_{hkl} can be calculated using DFT in the conventional way by evaluating the difference between the geometry-optimised supercell energy and that of the corresponding quantity of bulk material:

$$\gamma_{hkl}(n) = \frac{1}{2S}\left(E_{hkl}(n) - {}^{n}\!/_{2}\, E_B\right), \tag{2}$$

where E_B is the energy of the Ti_2O_4 bulk rutile unit cell, $E_{hkl}(n)$ is the geometry-optimised energy of a stoichiometric and symmetric Ti_nO_{2n} slab/vacuum supercell whose lattice vectors $\vec{A}$ and $\vec{B}$ lie in the high-index plane (hkl) and $2S$ is the total surface area per (symmetric and double-ended) supercell, given by $S = \left|\vec{A} \times \vec{B}\right|$. We emphasise the dependence of γ_{hkl} on the slab chemical formula Ti_nO_{2n} by writing $\gamma_{hkl} = \gamma_{hkl}(n)$. To create a structurally consistent set of high-index slabs, we choose a convention whereby the number of layers in a given slab, L, is defined in terms of n and we therefore use L as the independent variable.

By calculating the surface energy per unit area, γ_{hkl}, of three progressively higher index slab/vacuum supercells of L layers thickness using equation (2), and then substituting these values into equation (1), a system of three linear simultaneous equations is obtained whose solutions are $\gamma_{110}(L)$, $\beta(L)$ and $q(L)$. For example, (341), (451) and (561) slabs of L layers thickness hosting the $\langle 1\bar{1}1 \rangle$ step can be used to yield the surface energy per unit area values $\gamma_{341}(L)$, $\gamma_{451}(L)$ and $\gamma_{561}(L)$, which can then be substituted into equation (1) along with the corresponding step spacings d_{341}, d_{451}, d_{561} and vicinal surface misorientation angles θ_{341}, θ_{451} and θ_{561} taken directly from the supercell dimensions (see Supplementary Information Section 2). The resulting system of three linear simultaneous equations written in matrix form is

$$\begin{pmatrix} \gamma_{341}(L)/cos\theta_{341} \\ \gamma_{451}(L)/cos\theta_{451} \\ \gamma_{561}(L)/cos\theta_{561} \end{pmatrix} = \begin{pmatrix} 1 & d_{341}^{-1} & d_{341}^{-3} \\ 1 & d_{451}^{-1} & d_{451}^{-3} \\ 1 & d_{561}^{-1} & d_{561}^{-3} \end{pmatrix} \begin{pmatrix} \gamma_{110}(L) \\ \beta(L) \\ q(L) \end{pmatrix}, \tag{3}$$

and the solutions are

$$\gamma_{110}(L) = \frac{det\,G(L)}{det\,D}, \qquad \beta(L) = \frac{det\,B(L)}{det\,D}, \qquad q(L) = \frac{det\,Q(L)}{det\,D}, \tag{4}$$

where D is the matrix from equation (3) and $G(L)$, $B(L)$ and $Q(L)$ are matrices identical to D but whose first, second and third columns respectively have been replaced with the column vector of high-index surface energies from the left-hand side of equation (3), as per Cramer's determinant rule. This process can then be repeated for increasingly thick slabs of higher L, where the slabs' chemical formulae are increased according to a prescribed arithmetic rule, thereby exposing the behaviour of $\gamma_{110}(L)$, $\beta(L)$ and $q(L)$ with increasing L individually and consistently. The oscillatory behaviour of $\gamma_{hkl}(L)$ with increasing L propagates through to the solutions $\gamma_{110}(L)$, $\beta(L)$ and $q(L)$ so they also oscillate with increasing slab thickness and depend sensitively on L. The significant advantage of this approach is that the solutions $\gamma_{110}(L)$ can be cross-checked, for each and every value of L, with values calculated directly and separately using (110) slabs. We denote these directly calculated values $\tilde{\gamma}_{110}(L)$. The residual differences $\gamma_{110}(L) - \tilde{\gamma}_{110}(L)$ over the full range of L can then be analysed in order to determine whether the terrace component of the total high-index surface energy has been consistently extracted while naturally accounting for quantum size effects, therefore leaving the remaining step energies and interaction energies open to self-contained analysis. Expressed another way, it allows one to determine whether the macroscopic $\sim 1/d^2$ MP interaction potential accurately captures the true energetics of the atomistic slab models. This is important, because whilst the MP interaction potential appears to have been adopted by Gong et al.[40] and is frequently assumed and observed in the literature[51-54], there are also many instances in the literature[55-60] where atomic step-step interaction energies for various material surfaces have been observed or suggested to deviate from the $\sim 1/d^2$ behaviour due to atomistic effects.

2. THEORETICAL METHODS

2.1. Basis set, exchange correlation functional, bulk reference state and vacuum thickness

The plane wave density functional theory code CASTEP[61] was used with the GGA PBE exchange correlation functional[62] and Vanderbilt ultrasoft pseudopotentials[63] to converge the zero point energy of the bulk TiO_2 rutile unit cell with respect to the k point spacings s^i (where i denotes correspondence to the reciprocal vector b_i) and the kinetic energy cutoff E_C, where each was varied independently. This procedure yielded basis set values satisfying $s^i < 0.035\text{Å}^{-1}$ and

E_C = 400 eV, which were then used along with the GGA PBE functional for all subsequent calculations in the paper. Following this, a cell-optimised geometry optimisation calculation was carried out on the bulk unit cell with $P4_2/mnm$ symmetry imposed, in which the atomic forces were converged to within 0.01 eVÅ^{-1}. This stringent tolerance on the bulk cell was motivated by the high sensitivity of γ_{hkl} to the value of E_B in equation (2), and symmetry was imposed to avoid linear upscaling of any small deviations from the tetragonal lattice affecting the supercells built from the bulk cell. The bulk unit cell lattice parameters were recorded as $|\vec{a}| = 4.644$ Å (3 d. p.) and $|\vec{c}| = 2.966$ Å (3 d. p.), in good agreement with the experimentally measured[58] quantities $|\vec{a}|_{exp} = 4.594$ Å (3 d. p.) and $|\vec{c}|_{exp} = 2.959$ Å (3 d. p.). A three layer stoichiometric and symmetric (110) slab/vacuum Ti_60_{12} supercell was then built, whose surface-plane lattice vectors were fixed at values derived directly from the optimised bulk cell, and for which the vacuum thickness was fixed at magnitudes increasing in 1 Å increments from 3 Å to 12 Å inclusive, to make a total of 10 supercells. The geometry-optimised system energy was calculated for each, and a minimum vacuum thickness of 10 Å was identified in order to decouple all intercellular interactions along the vacuum direction. In all cases, the slab was placed in the centre of the vacuum.

2.2. Slab calculations

For the $\langle 001 \rangle_{Ti}$ step structure, (210), (320) and (430) slabs of 3,..., 10 layers ($L = 3, .., 10$) and P 1 2/m 1 symmetry were built to make a total of $8 \times 3 = 24$ slabs on which the terminations were cleaved manually to produce (110) terraces bounded by the $\langle 001 \rangle_{Ti}$ steps. This procedure was repeated for the $\langle 001 \rangle_{O}$ structure to make 24 more slabs, also of P 1 2/m 1 symmetry. For the $\langle 1\bar{1}1 \rangle$ and $\langle 1\bar{1}1 \rangle_R$ steps, (341), (451) and (561) slabs of 3,..., 10 layers ($L = 3, .., 10$) and $P\bar{1}$ symmetry were built to make $24 \times 2 = 48$ further slabs. For the $\langle 1\bar{1}1 \rangle_R$

slabs, the extra TiO_2 units were added manually to each end. Alongside these vicinal surfaces, 8 increasingly-thick symmetric and stoichiometric (110) slabs of 3,..., 10 layers were built for the consistency check. The total set of input files thus consisted of 104 slab/vacuum supercells. The projections onto the (110) plane of the supercells are shown in Figure 2. For each and every one of these 104 supercells, the surface-plane lattice vectors, $\vec{A}_{hkl}$ and $\vec{B}_{hkl}$ were fixed at values derived directly from the optimised bulk lattice parameters $|\vec{a}| = 4.644$ Å (3 d. p.) and $|\vec{c}| = 2.966$ Å (3 d. p.) as appropriate to each case. The surface-normal lattice vector $\vec{C}_{hkl}$ was fixed at a value such that the vacuum thickness always equalled or exceeded 10 Å and the crystal lattice was re-oriented with respect to the Cartesian coordinate system so that $\vec{C}_{hkl}$ was always aligned with the z axis. To maintain structural consistency, all high-index slabs were built such that the step on the top end of each slab was made to be situated directly opposite the step on the bottom end along the direction perpendicular to the (110) plane (up to a discrepancy of a bulk unit cell due to the AB stacking structure) as illustrated for the case of the $\langle 001 \rangle_{Ti}$ step in Figure 3.

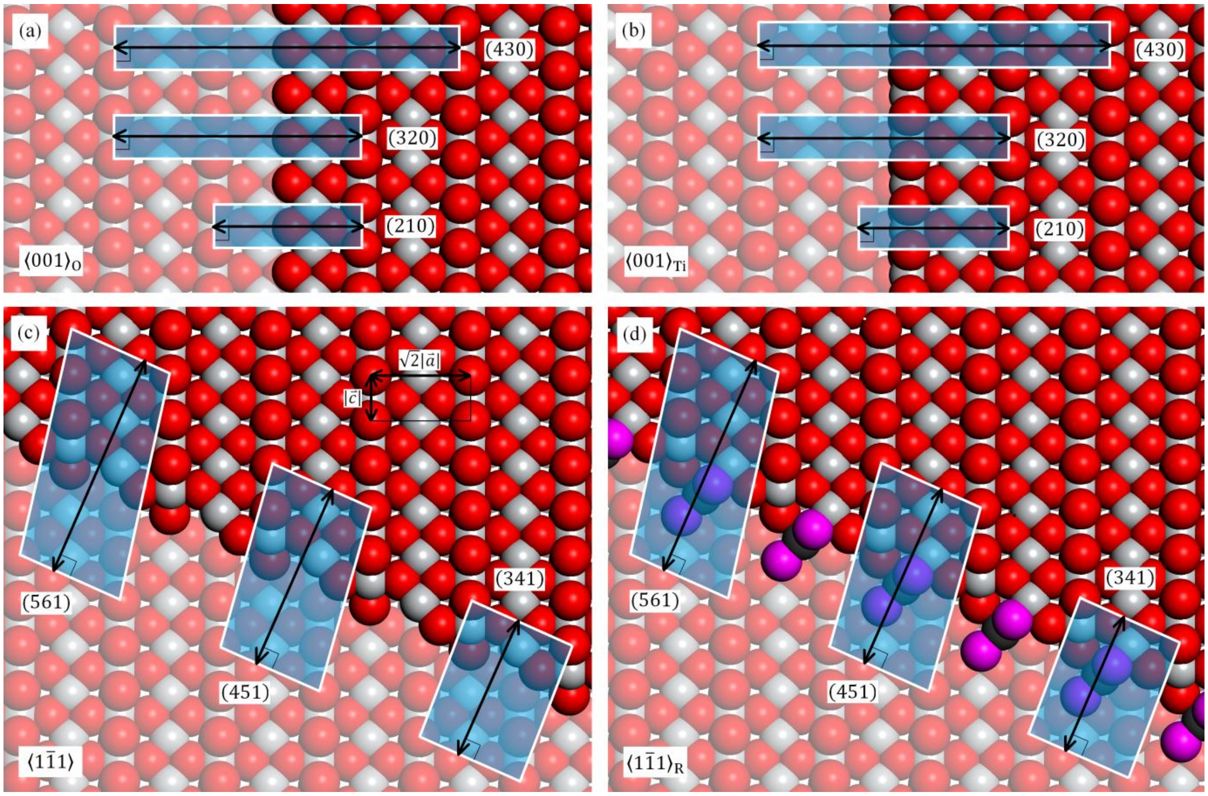

Figure 2. *Top-down views of the projection of the high-index supercells onto two terraces of a semi-infinite (110) surface bounded by (a)* $\langle 001\rangle_O$ *(b)* $\langle 001\rangle_{Ti}$ *(c)* $\langle 1\bar{1}1\rangle$ *and (d)* $\langle 1\bar{1}1\rangle_R$ *steps. The extra* TiO_2 *units of the* $\langle 1\bar{1}1\rangle_R$ *structure are depicted in purple and dark grey as in Figure 1. The distance measurements lying in the (110) plane indicated with black arrows are the step-step spacings* d_{hkl} *and the step height in all cases is* $\sqrt{2}|\vec{a}|$. *The supercells used in the corresponding DFT calculations were built double-ended with vacuum slabs in the infinite periodic regime like those illustrated in Figure 3.*

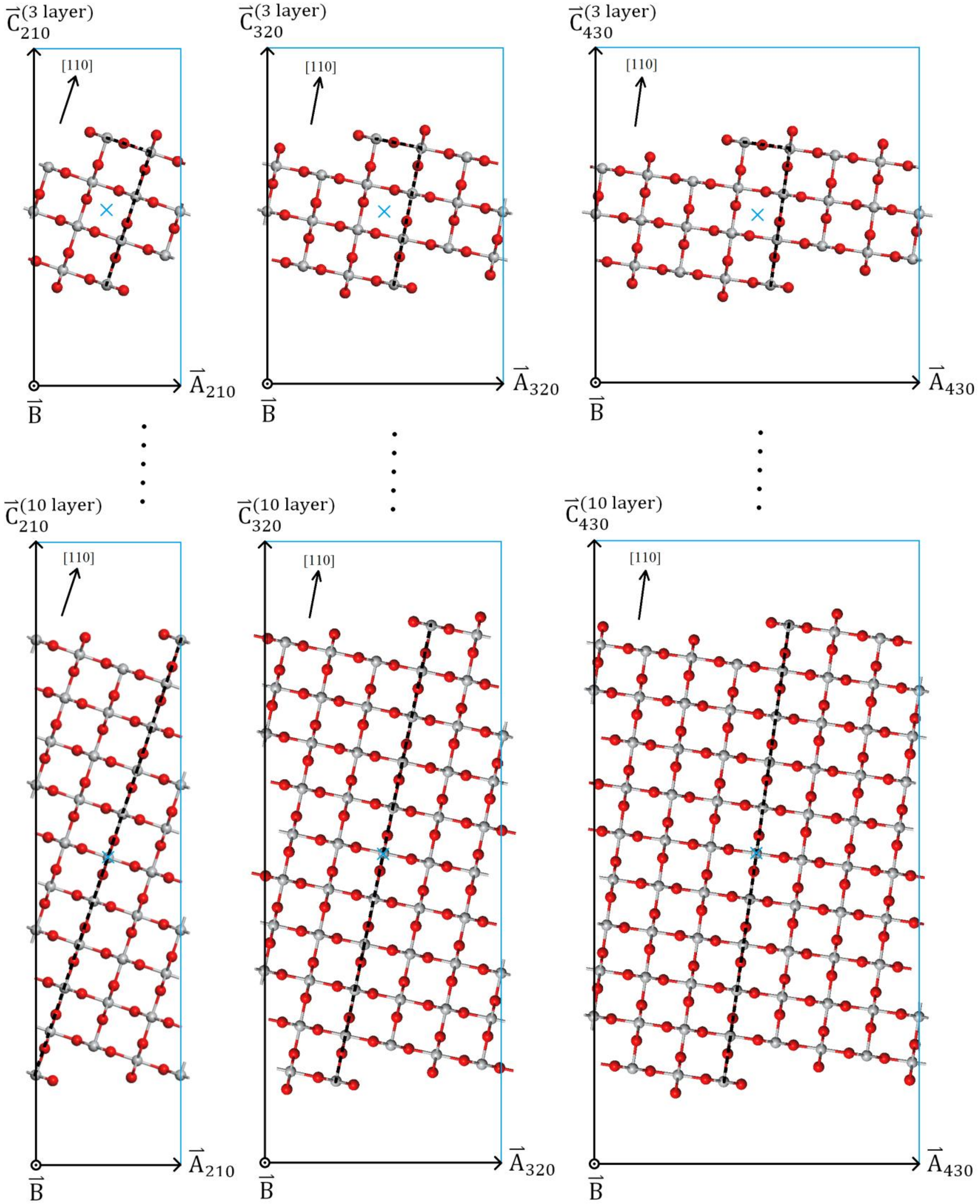

Figure 3. *Side views of the set of 24 supercells used for the* $\langle 001 \rangle_O$ *step using ball and stick representation. All supercells have inversion symmetry about the centroid located at fractional*

coordinates (0.5, 0.5, 0.5), indicated in each supercell with the blue cross. The two steps on the opposing ends of every slab in the entire set of input files are consistently located either i) directly opposite each other along the direction [110], for L = even cases , or ii) opposite each other along the direction [110], up to a discrepancy of a single unit cell for L = odd cases. This is indicated by the black dotted lines joining the opposing steps for the supercells shown.

Step	Slab Miller index	Number of layers, L, defined by chemical formula Ti_nO_{2n}			Step	Slab Miller index	Number of layers, L, defined by chemical formula Ti_nO_{2n}	
		Even L	Odd L				Even L	Odd L
$\langle 001\rangle_{Ti}$	(210)	$Ti_{3L+1}O_{2(3L+1)}$	$Ti_{3L+2}O_{2(3L+2)}$		$\langle 001\rangle_{O}$	(210)	$Ti_{3L+1}O_{2(3L+1)}$	$Ti_{3L+2}O_{2(3L+2)}$
	(320)	$Ti_{5L+1}O_{2(5L+1)}$	$Ti_{5L+2}O_{2(5L+2)}$			(320)	$Ti_{5L+1}O_{2(5L+1)}$	$Ti_{5L+2}O_{2(5L+2)}$
	(430)	$Ti_{7L+1}O_{2(7L+1)}$	$Ti_{7L+2}O_{2(7L+2)}$			(430)	$Ti_{7L+1}O_{2(7L+1)}$	$Ti_{7L+2}O_{2(7L+2)}$
$\langle 1\bar{1}1\rangle$	(341)	$Ti_{7L+3}O_{2(7L+3)}$	$Ti_{7L+2}O_{2(7L+2)}$		$\langle 1\bar{1}1\rangle_{R}$	(341)	$Ti_{7L+5}O_{2(7L+5)}$	$Ti_{7L+4}O_{2(7L+4)}$
	(451)	$Ti_{9L+2}O_{2(9L+2)}$	$Ti_{9L+3}O_{2(9L+3)}$			(451)	$Ti_{9L+4}O_{2(9L+4)}$	$Ti_{9L+5}O_{2(9L+5)}$
	(561)	$Ti_{11L+3}O_{2(11L+3)}$	$Ti_{11L+2}O_{2(11L+2)}$			(561)	$Ti_{11L+5}O_{2(11L+5)}$	$Ti_{11L+4}O_{2(11L+4)}$

Table 1. The convention used to define the number of layers, L, in terms of the number of TiO_2 units, n. For example, a 6 layer (320) slab hosting a $\langle 001\rangle_{Ti}$ step on each end has chemical formula $Ti_{31}O_{62}$. By using this convention, all four sets of slabs were structurally consistent with each other as exemplified in Figure 3.

This structural convention was encoded arithmetically in terms of the slabs' chemical formulae and summarised in Table 1. CASTEP[61] was then used with the GGA PBE functional[62] and Vanderbilt ultrasoft pseudopotentials[63] to carry out a geometry optimisation calculation on these 104 supercells in which all atomic positions were allowed to relax in all directions. For each series of self-consistent field (SCF) cycles used for the electronic minimisation, the exit criterion was imposed that the change in total electron energy between successive SCF cycles be less than 5×10^{-7} eV three times in succession. For the geometry optimisation, the low memory Broyden–Fletcher–Goldfarb–Shanno (LBFGS) optimisation algorithm[65-70] was used with the following 3 exit criteria: i) that the maximum force on all atoms be less than 0.03 eVÅ^{-1}, ii) that the maximum change in position for all atoms between successive LBFGS steps be less than 10^{-3} Å and iii) that the maximum change in the total system energy between successive LBFGS steps be less than 10^{-5} eV per atom.

The total electron density slices of the fully relaxed slabs were then examined, some of which are presented in Figure 4. The 96 fully-optimised supercell energies E_{hkl} were inserted as appropriate with the bulk energy E_B into equation (1) to yield the surface energy per unit area of the high index surface for each slab, $\gamma_{hkl}(L)$, and these values were plotted against L in Figure 5 and tabulated in Table 2. These values were then substituted as appropriate into equation (2), and the resulting systems of simultaneous equations were solved to find the solutions $\gamma_{110}(L)$, $\beta(L)$ and $q(L)$ with increasing L for each of the four steps as explained in section 1.4. For each step, the solutions $\gamma_{110}(L)$ were plotted against the $\tilde{\gamma}_{110}(L)$ values calculated directly using the (110) slabs in Figure 6 for the consistency check, along with the residuals $\mathit{\Delta}\gamma_{110}(L) = \gamma_{110}(L) - \tilde{\gamma}_{110}(L)$. The solutions $\beta(L)$ and $q(L)$ were plotted in Figures 6 and 7 respectively and tabulated in Table 2.

3. RESULTS AND ANALYSIS

3.1. Initial remarks

All 104 slabs relaxed into a configuration corresponding to an energetic minimum. It can be seen from the total electron density slices in Figure 4 that the interlayer interactions (and interlayer distances) depend critically on the number of layers in the slab. The dominant electronic orbitals which contribute to this effect are Ti $3d$ and O $2p$ states, which we confirmed for all of our slabs with angular momentum-resolved density of states plots and orbital density plots. This is exactly what was observed and explained in detail for the case of TiO_2 rutile (110) slabs by Bredow et al.[34] Electron density slices 1 and 2 shown in Figure 4 (h) for (110) slabs look virtually identical to those presented by Bredow et al. The high-index surface energies $\gamma_{hkl}(L)$ plotted in Figure 5 display oscillatory convergence with increasing L. This is the direct consequence of the alternating configurations of electron density as seen in Figure 4. It is also the physical reason why the method of using linear regression to estimate the surface energy from the intercept of a plot of total supercell energies against n (refuted in detail in Section 1 of the Supporting Information) is unsuitable for the case of TiO_2 rutile, or indeed any material in which surface-surface interactions are strong. We emphasise at this point that the oscillations in Figure 5 are not merely a consequence of artificial aspects of the calculation; in particular, the different k points sampling grid used for the calculation of the bulk unit cell energy, E_B, from that of each total supercell energy, E_{hkl}. This was verified directly by calculating values of E_B using new (and substantially larger) bulk unit cells for selected slabs, where the lattice parameters of these bulk cells were systematically chosen so that the k point sampling grids in each case was identical to that of the corresponding slab/vacuum supercell. The resulting surface energies were the same to 7 significant figures and showed identical oscillations. This confirms, for the avoidance of any doubt, that the different sampling grid used for the bulk cell is of no consequence, and moreover that the basis set used throughout all our calculations is robust and fully converged.

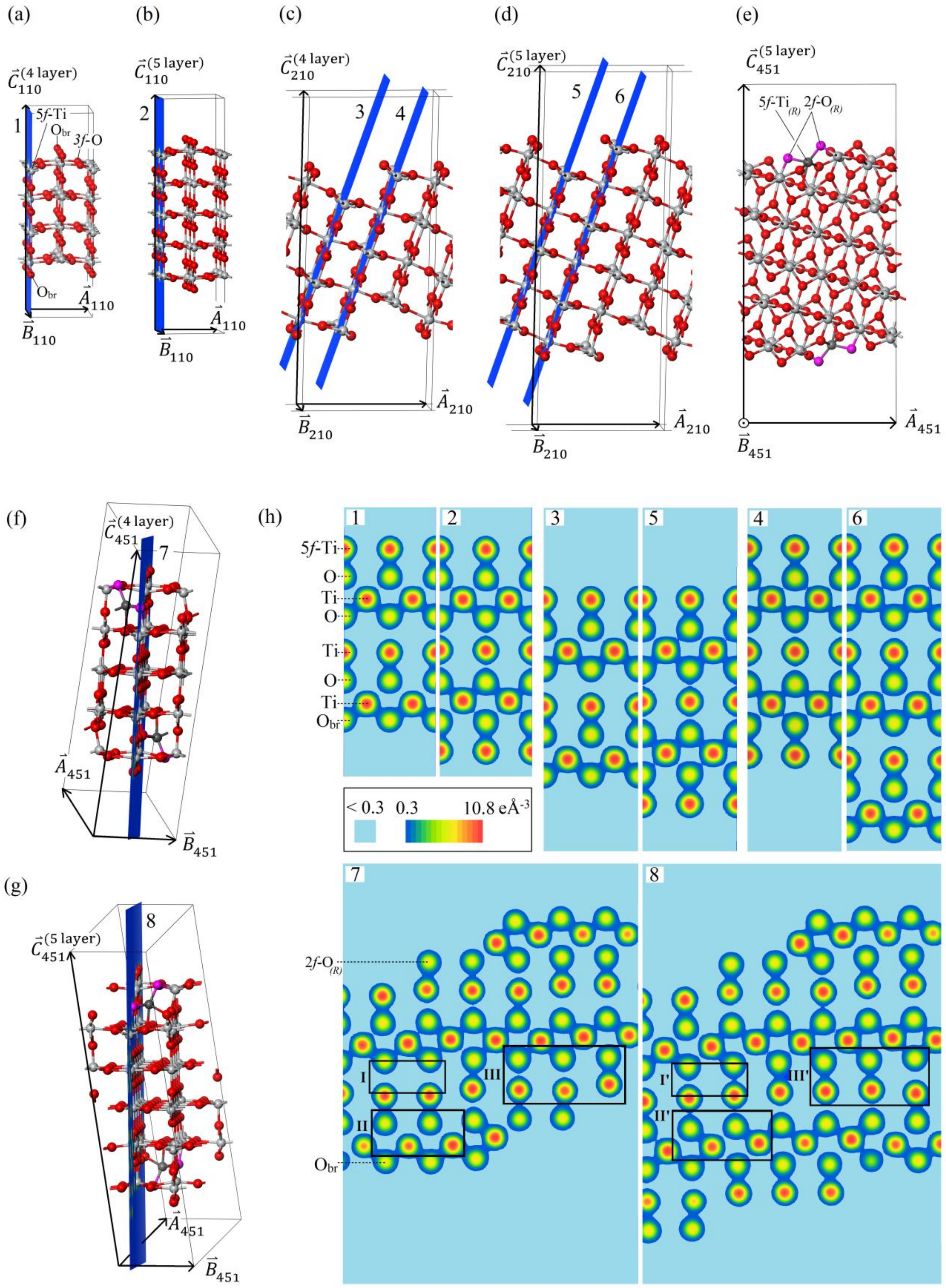
(a)
(b)
(c)
(d)
(e)
$\vec{C}_{110}^{(4\ \text{layer})}$
$\vec{C}_{110}^{(5\ \text{layer})}$
$\vec{C}_{210}^{(4\ \text{layer})}$
$\vec{C}_{210}^{(5\ \text{layer})}$
$\vec{C}_{451}^{(5\ \text{layer})}$
1
2
3
4
5
6
5f-Ti
O_{br}
3f-O
O_{br}
$5f\text{-Ti}_{(R)}$
$2f\text{-O}_{(R)}$
$\vec{A}_{110}$
$\vec{B}_{110}$
$\vec{A}_{110}$
$\vec{B}_{110}$
$\vec{A}_{210}$
$\vec{B}_{210}$
$\vec{A}_{210}$
$\vec{B}_{210}$
$\vec{A}_{451}$
$\vec{B}_{451}$
(f)
$\vec{C}_{451}^{(4\ \text{layer})}$
7
$\vec{A}_{451}$
$\vec{B}_{451}$
(g)
$\vec{C}_{451}^{(5\ \text{layer})}$
8
$\vec{A}_{451}$
$\vec{B}_{451}$
(h)
1
2
3
5
4
6
5f-Ti
O
Ti
O
Ti
O
Ti
O_{br}
< 0.3
0.3
10.8 eÅ^{-3}
7
8
$2f\text{-O}_{(R)}$
O_{br}
I
II
III
I'
II'
III'

Figure 4. *The physical reason for the oscillations in the energetic components plotted in Figures 5, 6 and 7: thickness-dependent alternating configurations of electron density. (a) Ball and stick models of (a) 4 layer and (b) 5 layer (110) slabs with electron density slices passing through 5f-Ti surface atoms. (c) Ball and stick model of a 4 layer (210) /* $\langle 001\rangle_O$ *slab, (d) a 5 layer (210) /* $\langle 001\rangle_O$ *slab. (e) Side view of a 5 layer (451) /* $\langle 1\bar{1}1\rangle_R$ *slab. (f) Ball and stick model of (f) 4 layer (451) /* $\langle 1\bar{1}1\rangle_R$ *slab and (g) 5 layer (451) /* $\langle 1\bar{1}1\rangle_R$ *slab. In all ball and stick models, Ti atoms are illustrated in grey and O in red. For the* $\langle 1\bar{1}1\rangle_R$ *models, the extra Ti atoms are shown in dark grey, and the extra O in purple. (h) Electron density slices from (a) - (f) in units of electrons /* $Å^3$. *For slices 1 and 2, the interlayer distances between the 4th/5th and 5th/6th atomic layer from the top are quite different. The interlayer distances from slices 3 and 5, and from slices 4 and 6 in the (210) slabs show similar traits. In slices 7 and 8, the regions I/I', II/II' and III/III' are outlined where slab thickness-dependent alternating modes of electron density are most evident.*

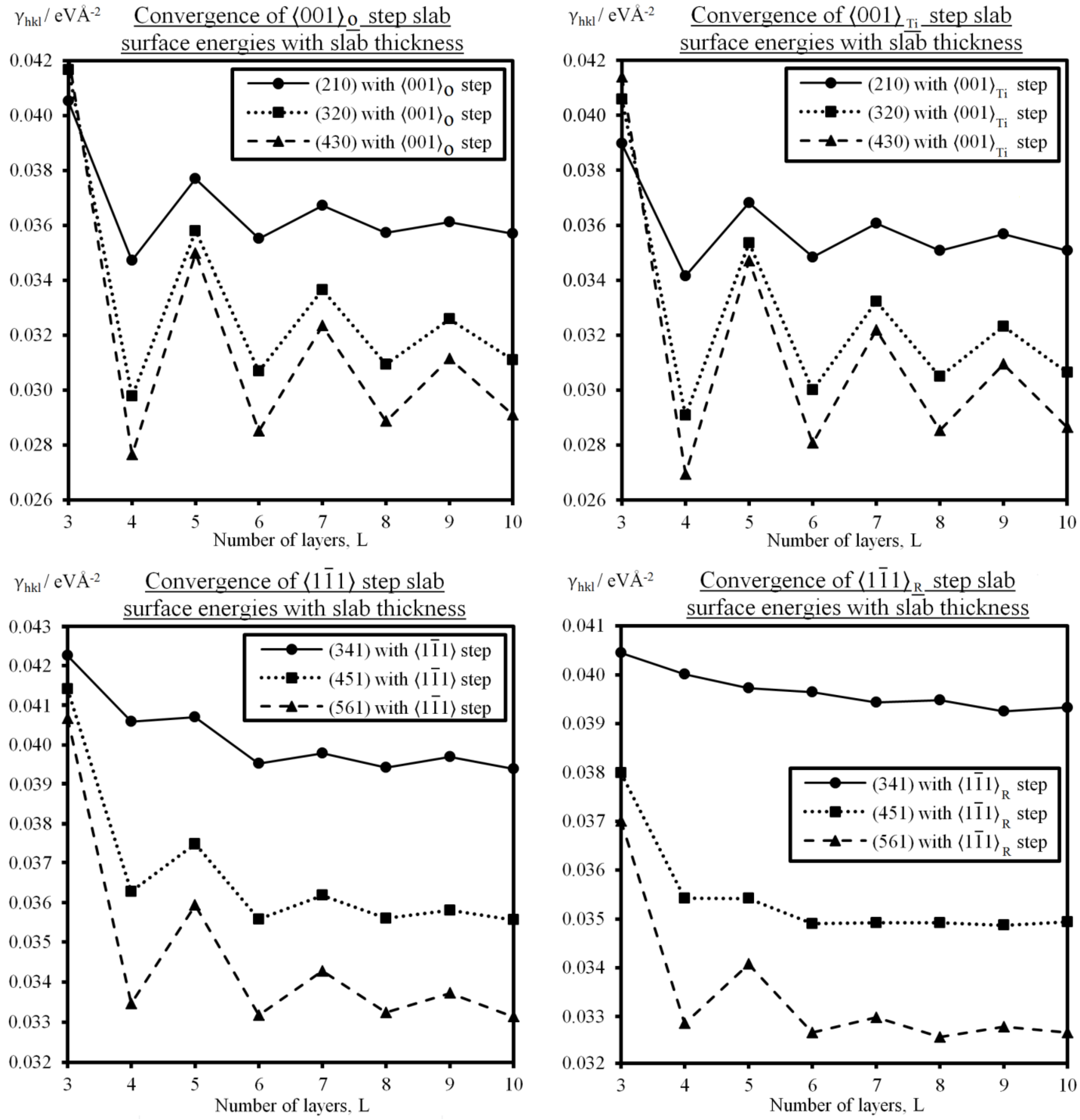

Figure 5. *The convergence of surface energy per unit area with slab thickness. Despite the clear oscillations due to alternating modes of electron density, the surface energies clearly converge to finite values. In all but a few* $L = 3$ *cases, higher index surfaces have lower surface energy per unit area.*

It can be seen that these oscillations propagate through to the solutions γ_{110}, β and q plotted in Figures 6, 7 and 8 respectively, and the magnitude of the residual oscillations in these solutions is large compared to the values themselves.

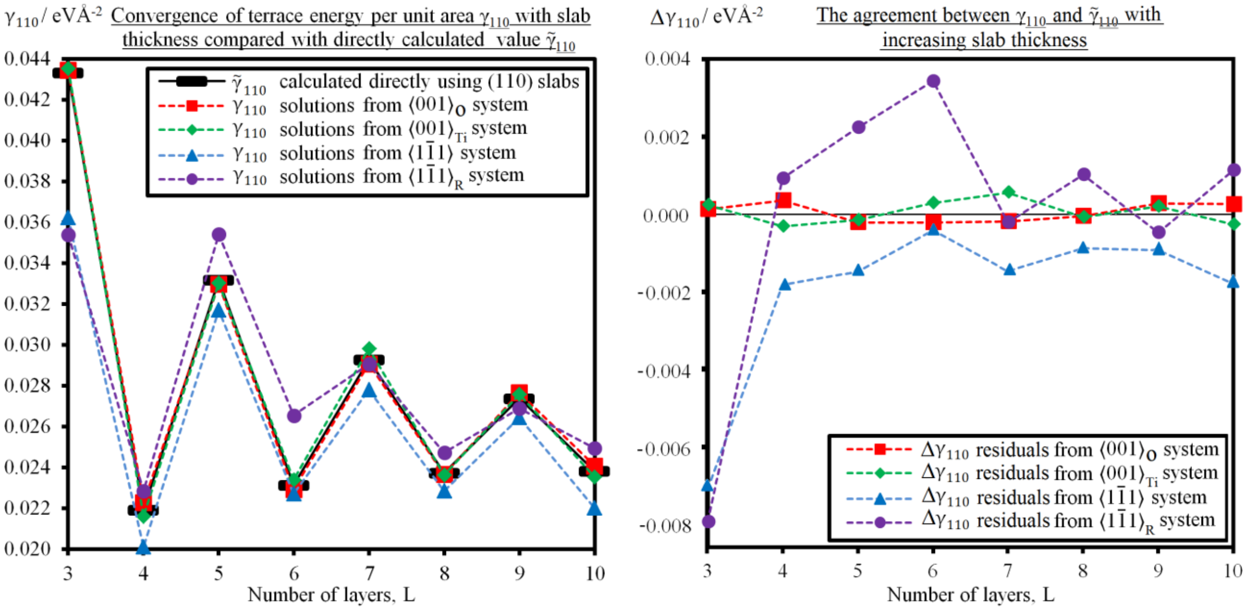

Figure 6. ***Left panel:*** *The convergence of the (110) terrace energy per unit area for the four steps, compared with the values calculated directly using (110) slabs.* ***Right panel:*** *The residual differences* $\Delta\gamma_{110}(L) = \gamma_{110}(L) - \tilde{\gamma}_{110}(L)$ *which show the validity of applying equation (1) to the atomistic supercells used.*

Currently, *ab initio* calculations are generally impractical for supercells exceeding the size of those used in this study, and so to draw comparisons between the solutions γ_{110}, β and q with experimental observations of laboratory samples of finite but macroscopic thickness, one must rely on an extrapolation of the plots along the direction $+L$ towards $L \to \infty$. This demonstrates the challenge involved with calculating accurate step energies for macroscopically thick crystals.

There is also a small statistical uncertainty in the fully optimised supercell energies E_{hkl} which originates from the finite tolerances used in the geometry optimisation. This uncertainty is common to the $\langle 1\bar{1}1\rangle$, $\langle 1\bar{1}1\rangle_R$, $\langle 001\rangle_{Ti}$ and $\langle 001\rangle_O$ systems. The $\langle 1\bar{1}1\rangle$ and $\langle 1\bar{1}1\rangle_R$ slabs are substantially lower in symmetry than those of the $\langle 001\rangle_{Ti}$ and $\langle 001\rangle_O$ systems, so this source of uncertainty is likely to be more severe for these systems. The reader is referred to Section 3 of the Supporting Information for a discussion of these sources of statistical uncertainty. We note that the values $\tilde{\gamma}_{110}(L)$ agree well with published calculations.[35-37]

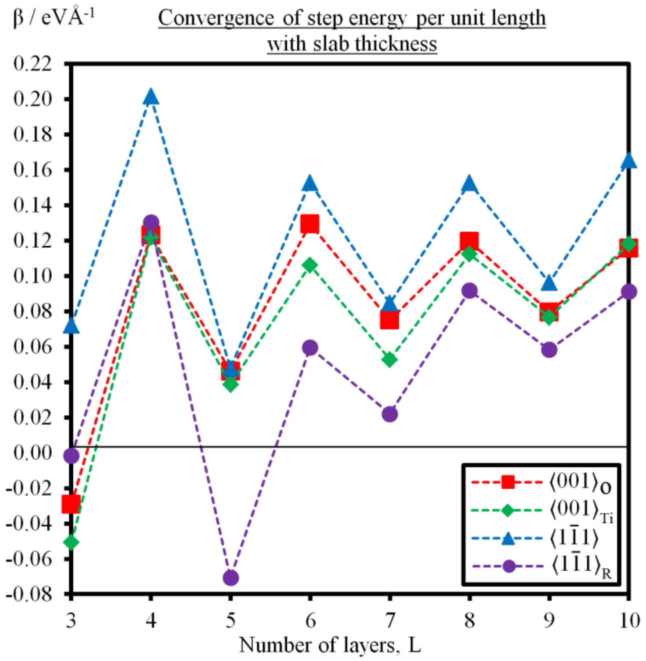

Figure 7. *The convergence of step energy per unit length with increasing slab thickness for the four steps studied. Despite the large oscillations in the solutions, it is quite clear that the* $\langle 1\bar{1}1\rangle_R$ *step is the most stable.*

Step	Number of layers, L	Slab surface energy per unit area of (hkl) plane, γ_{hkl} / eVÅ^{-2} × 10^{-2} (3 d. p.)			(110) terrace surface energy per unit area, γ_{110} / eVÅ^{-2} × 10^{-2} (3 d. p.)	Step energy per unit length, β / eVÅ^{-1} (3 d. p.)	Step-step interaction constant, q / eVÅ (3 d. p.)
		γ_{210}	γ_{320}	γ_{430}			
$\langle 001\rangle_{\mathrm{O}}$	3 layer	3.845	4.086	4.175	4.344	-0.029	0.066
	4 layer	3.294	2.919	2.736	2.229	0.123	-0.057
	5 layer	3.577	3.510	3.463	3.298	0.046	0.052
	6 layer	3.370	3.009	2.822	2.292	0.129	-0.498
	7 layer	3.483	3.300	3.202	2.908	0.075	0.024
	8 layer	3.390	3.033	2.857	2.367	0.120	-0.057
	9 layer	3.427	3.196	3.084	2.766	0.080	0.370
	10 layer	3.387	3.048	2.881	2.408	0.116	-0.110
$\langle 001\rangle_{\mathrm{Ti}}$	3 layer	3.697	3.980	4.098	4.355	-0.051	0.535
	4 layer	3.240	2.852	2.667	2.162	0.122	0.155
	5 layer	3.492	3.467	3.436	3.304	0.039	-0.149
	6 layer	3.305	2.942	2.779	2.341	0.106	0.649
	7 layer	3.421	3.258	3.187	2.983	0.053	0.843
	8 layer	3.327	2.990	2.825	2.364	0.112	0.021
	9 layer	3.385	3.169	3.063	2.759	0.077	0.299
	10 layer	3.328	3.005	2.836	2.355	0.118	-0.431
		γ_{341}	γ_{451}	γ_{561}			
$\langle 1\bar{1}1\rangle$	3 layer	3.992	3.998	3.972	3.624	0.072	-1.352
	4 layer	3.834	3.503	3.266	2.011	0.201	-0.690
	5 layer	3.846	3.620	3.509	3.171	0.048	3.351
	6 layer	3.735	3.436	3.238	2.271	0.153	0.574
	7 layer	3.759	3.494	3.347	2.780	0.085	2.580
	8 layer	3.725	3.438	3.245	2.285	0.153	0.383
	9 layer	3.751	3.457	3.292	2.645	0.096	2.612
	10 layer	3.721	3.434	3.234	2.203	0.165	-0.095
$\langle 1\bar{1}1\rangle_{\mathrm{R}}$	3 layer	3.774	3.619	3.565	3.539	-0.002	4.000
	4 layer	3.733	3.372	3.160	2.286	0.130	2.452
	5 layer	3.706	3.371	3.279	3.542	-0.071	9.553
	6 layer	3.698	3.322	3.142	2.655	0.059	5.350
	7 layer	3.678	3.323	3.172	2.906	0.022	6.400
	8 layer	3.683	3.323	3.133	2.474	0.092	3.853
	9 layer	3.661	3.318	3.153	2.691	0.058	4.808
	10 layer	3.668	3.325	3.142	2.495	0.091	3.599
		$\tilde{\gamma}_{110}$					
pristine (110) surface	3 layer	4.332	-	-	-	-	-
	4 layer	2.194	-	-	-	-	-
	5 layer	3.319	-	-	-	-	-
	6 layer	2.313	-	-	-	-	-
	7 layer	2.927	-	-	-	-	-
	8 layer	2.373	-	-	-	-	-
	9 layer	2.739	-	-	-	-	-
	10 layer	2.382			-	-	-

Table 2. The (110) terrace surface energy per unit area, step energy per unit length and step-step interaction constant on the four vicinal surface types.

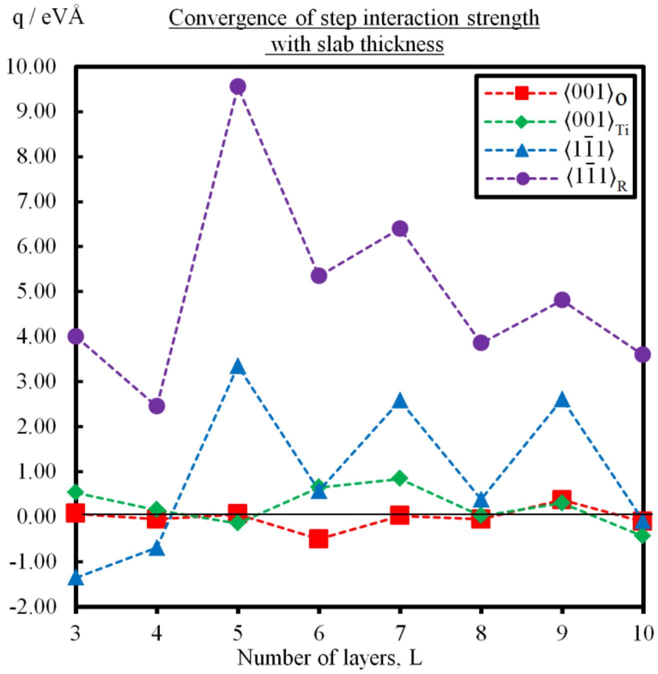

Figure 8. *The convergence of the step-step interaction constant with increasing slab thickness for the four steps studied. Despite the large oscillations in the plot, the* $\langle 001\rangle_O$ *and* $\langle 001\rangle_{Ti}$ *steps clearly have the weakest interactions, and the* $\langle 1\bar{1}1\rangle_R$ *step has the strongest interactions.*

3.2. $\langle 001\rangle_{Ti}$ and $\langle 001\rangle_O$ steps

The γ_{110} solutions extracted from the $\langle 001\rangle_{Ti}$ and $\langle 001\rangle_O$ systems show excellent agreement with the $\tilde{\gamma}_{110}$ values which suggests that the q/d^3 interaction term in equation (1) was a good guess. This result shows that the (110) terrace component of the total high-index surface energy has been accurately extracted for the $\langle 001\rangle_{Ti}$ and $\langle 001\rangle_O$ steps for all slab thicknesses, leaving the corresponding solutions $\beta(L)$ and $q(L)$ open to physical analysis. Martinez et al.[23] suggested from their total supercell energy calculations that the $\langle 001\rangle_{Ti}$ and $\langle 001\rangle_O$ steps were very similar in energy. Figure 7 shows that the step energies per unit length are likely to converge towards about β =0.10 ± 0.02 eVÅ^{-1} for both steps as $L \rightarrow \infty$, where these precision uncertainties have been estimated by merely examining the plots around the region $L = 9{,}10$. They are indeed therefore very similar, at least up to $L = 10$, and so this suggests that both structures may be likely to occur on laboratory samples in equal proportions. Diebold observed some instances of reconstructions on $\langle 001 \rangle$-type steps[20] on annealed rutile (110) and this observation could perhaps be due to symmetry breaking caused by a stalemate in the formation of the energetically very similar $\langle 001 \rangle_{Ti}$ and $\langle 001 \rangle_{O}$ steps. The $\langle 001 \rangle_{Ti}$ and $\langle 001 \rangle_{O}$ structures clearly have very weak interactions with themselves, indicating that both structures induce a negligible strain field throughout the surface region of the crystal. The residual variations in the q solutions are of magnitude ~ 1 eVÅ. With regards these variations, it is not possible to reliably rule out the possible intrinsic sources of (small) uncertainty in the DFT calculations, including the slabs relaxing into metastable minima and the statistical uncertainty of the final energy values owing to the finite energy change tolerance of 10^{-5} eV per atom. We therefore conclude that the interaction energies of the $\langle 001 \rangle_{Ti}$ and $\langle 001 \rangle_{O}$ steps are zero to the level of precision attainable from our calculations.

3.3. $\langle 1\bar{1}1 \rangle$ and $\langle 1\bar{1}1 \rangle_R$ steps: general comments

Steps extended along the directions $\langle 1\bar{1}1 \rangle$ comprise the vast majority of all step defects on rutile (110), so determining which of these two structures studied is the most energetically stable is of particular interest. The solutions γ_{110} extracted from the $\langle 1\bar{1}1 \rangle$ and $\langle 1\bar{1}1 \rangle_R$ systems recover the oscillatory manner of convergence but they display some slight deviations from the $\tilde{\gamma}_{110}$ data. The corresponding sets of supercells used for these two systems have identical dimensions, and they differ only in that they contain different arrangements of atoms at the steps. Therefore, besides considerations relating to the small uncertainty resulting from the geometry optimised energy values, the distinct behaviour of these two systems is completely attributable to the two distinct steps. The task at hand therefore is to attempt to itemise and disentangle the factors of physical origin in order to try and explain the discrepancies and gain an indication of the true energies of these steps. In the following two sections, we discuss the data for the $\langle 1\bar{1}1\rangle_R$ step and $\langle 1\bar{1}1\rangle$ step seperately. Firstly, $\langle 1\bar{1}1\rangle_R$:

3.4. $\langle \mathbf{1\bar{1}1}\rangle_R$ step: detailed analysis

The trend in the residual differences $\Delta\gamma_{110}$ for the $\langle 1\bar{1}1\rangle_R$ step show that the γ_{110} values are a very slight overestimation of $\tilde{\gamma}_{110}$ for the thickest slabs and severe underestimation of $\tilde{\gamma}_{110}$ for the $L = 3$ slabs. We have identified two possible contributing factors of physical origin: *i)* interactions between neighbouring steps which were not accounted for by equation (1), and which may themselves depend on L in a non-simple way, and *ii)* surface-surface interactions between steps on opposing surfaces of the slab which also depend non-trivially on L. Both of these factors are likely to be making significant contributions to the true interaction energy and therefore producing a systematic error resulting in overvaluations and undervaluations of the γ_{110} solutions.

The obvious candidate for the origin of atomistic contributions to the interaction between neighbouring steps is the set of (341) slabs with the $\langle 1\bar{1}1\rangle_R$ step. The small step width approximation is less well founded for these systems, which can be appreciated by referring to Figure 2 (d) which shows that the width of the step structure is significant compared to the size of the lower (110) terrace region. This is in contrast to the $\langle 001\rangle$ systems for which the approximation is clearly a good one. In fact, there is an indication with the data available in Figure 6 that interactions between step on opposing surfaces of the slab are likely to be the dominating factor, especially at small L. Observe the differences between $\gamma_{110}(L)$ and $\tilde{\gamma}_{110}(L)$ at $L = 3$: both the $\langle 1\bar{1}1\rangle_R$ and the $\langle 1\bar{1}1\rangle$ systems produce values of $\gamma_{110}(3)$ which are very large underestimates of $\tilde{\gamma}_{110}(3)$. The sets of $\langle 1\bar{1}1\rangle_R$ and $\langle 1\bar{1}1\rangle$ slabs at $L = 3$ of course have different steps, but they have small surface-surface distances in common. Furthermore, in the higher L range $L = 7$, ...,10, the agreement between γ_{110} and $\tilde{\gamma}_{110}$ for the $\langle 1\bar{1}1\rangle_R$ step is quite good. The residuals $\Delta\gamma_{110}$ at large L are just about small enough to be plausibly accounted for by the intrinsic uncertainties in the supercell energies. The indication therefore is that choosing the q/d^3 interaction term in equation (1) results in an accurate simulation of the interactions between $\langle 1\bar{1}1\rangle_R$ steps, but only once surface-surface interactions have been decoupled at large slab thicknesses. The instances where β is predicted to be negative ($L = 3$, 5) indicate that equation (1) fails for the purposes of extracting the energetics of neighbouring steps because of the significant influence of surface-surface step interactions in the thinner slabs.

In summary, Figure 7 shows that β for the $\langle 1\bar{1}1\rangle_R$ step on macroscopically thick samples is likely to fall approximately within the range β = 0.07 ± 0.02 $\text{eV}\text{Å}^{-1}$ for $L \to \infty$, and Figure 8 similarly shows that these steps on vicinal surfaces exhibit a repulsive interaction consistent with a positive interaction constant q falling in the range of about 4 ± 2 eVÅ as $L \to \infty$.

3.5. $\langle 1\bar{1}1\rangle$ step: detailed analysis

Now observe the γ_{110} solutions for the $\langle 1\bar{1}1\rangle$ step: some variation remains, but each and every one of the 8 solutions γ_{110} is undervalued compared to $\tilde{\gamma}_{110}$. Surface-surface interactions are probably making major contributions at small L due to the clear disagreement of $\gamma_{110}(3)$ with $\tilde{\gamma}_{110}(3)$ as explained in the previous section. However the underestimation of the value of γ_{110} at $L = 10$ value is probably too large for intrinsic the uncertainty in the supercell energy to be a plausible cause. Besides the possibility of an unlikely and spurious cancellation of other unconsidered factors, this indicates that atomistic interaction terms may be contributing to the interaction energy for the $\langle 1\bar{1}1\rangle$ step, resulting in a systematic error originating from the false assumption that the step interaction is completely described by a term of the form q/d^3. To provide an approximate indication of what the true overall interaction scaling behaviour is, equation (1) was rewritten with an interaction term of the form q/d^m and successive iterations on the value of m were carried out to minimise the sum of the squares of the residual differences between the solutions $\gamma_{110}(L)$ and the values $\tilde{\gamma}_{110}(L)$ over the range $L = 7,..,10$. This range was chosen in a basic attempt to try and filter out surface-surface interactions. The best fit result was m = 2.14 (3 s. f.), consistent with an overall step-step interaction energy which scales as $1/d^{1.14}$. (This was then cross-checked by carrying out the same procedure on the $\langle 1\bar{1}1\rangle_R$ data, and the result was m = 3.13, implying an overall interaction energy scaling behaviour of $\sim 1/d^{2.13}$ which is in good agreement with the originally nominated $\sim 1/d^2$ MP interaction potential.) The corresponding values of β for $\langle 1\bar{1}1\rangle$ with this $q/d^{2.14}$ interaction term remained relatively unchanged and were still substantially larger than those from the $\langle 1\bar{1}1\rangle_R$ system. Therefore, no pivotal implications for the theoretical probing of STM images emerge from this because the $\langle 1\bar{1}1\rangle_R$ step is still implied to be vastly energetically favourable.

3.6. Comparison with published STM data

In Figure 9, we reproduce STM data from Martinez et al.[21] showing the annealed rutile (110) surface. Alongside this, a series of 2D Wulff constructions with increasing L is presented in which we have assumed two island morphologies: *i)* a (110) terrace bound by $\langle 1\bar{1}1\rangle$ steps and $\langle 001\rangle_{Ti}$ steps and *ii)* a (110) terrace bound by $\langle 1\bar{1}1\rangle_R$ steps and $\langle 001\rangle_{Ti}$ steps. By drawing vectors from a common origin whose directions are perpendicular to the step in question and whose lengths are drawn in proportion to the corresponding β values, the island shapes predicted to occur on the surface as a function of increasing slab thickness can be directly compared with the island seen in the STM image.

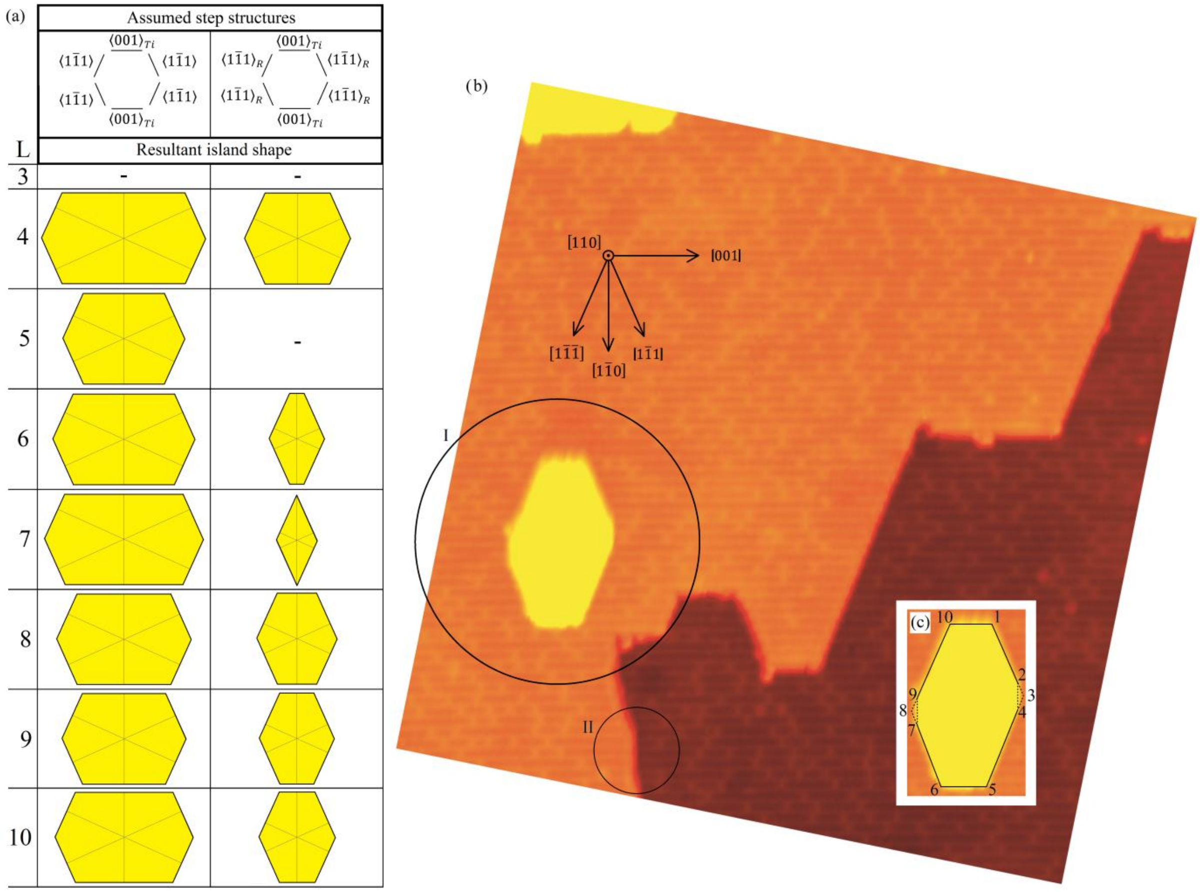

Figure 9. *(a) Terrace island shapes predicted using Wulff constructions in 2 dimensions using the* $\beta(L)$ *values (*$L = 3,..,10$*) plotted in Figure 7 assuming a (110) terrace bound by i)* $\langle 001\rangle_{Ti}$ *with* $\langle 1\bar{1}1\rangle$ *steps and ii)* $\langle 001\rangle_{Ti}$ *with* $\langle 1\bar{1}1\rangle_R$ *steps. (b) Terrace island on rutile (110) surface (circle I.) observed using STM carried out in a UHV chamber at 120 - 140 K in constant current mode with a tunneling voltage of approximately + 1.25 V. An instance of an apparent* $\langle 1\bar{1}0\rangle$*-type step is indicated in circle II. (c) Further features of the island not accounted for by this work. The kinks labeled 1 - 10 and their locations relative to each other show the apparent chirality of the island, and the possibility of* $\langle 1\bar{1}0\rangle$*-type edges existing on the island. STM image reproduced from Ref. 21 with kind permission of S. Wendt.*

An island of unquestionable similarity on an annealed rutile (110) sample was also observed by Diebold et al.[20] It is evident that the island shape predicted with a $\langle 1\bar{1}1\rangle/\langle 001\rangle_{Ti}$ morphology is inconsistent with the observed island shape for all values of L. In contrast, the $\langle 1\bar{1}1\rangle_R/\langle 001\rangle_{Ti}$ morphology (or indeed $\langle 1\bar{1}1\rangle_R/\langle 001\rangle_O$, which are not drawn but look very similar) produces an island shape which converges quite convincingly to that seen in experiments[19-21] by approximately 8 layers thickness and beyond. The predictions are clearly less reliable for slab thicknesses of less than about 7 layers. This demonstrates the predictive power of the methodology and adds credibility to the existence of the $\langle 1\bar{1}1\rangle_R$ step structure on laboratory samples. Instances which included negative β values for one or both steps (3 and 5 layer cases) were not included in the Wulff constructions.

It is clear that there are features on the surface shown in Figure 9 (b) which are not predicted or accounted for by the level of theory we have presented in this work. It is necessary to review these features to validate any claims of correspondence between theory and experiment, and also to try to anticipate how our approach may be refined. Firstly, by basing our approach on surface energies calculated via reference to a stoichiometric bulk state as in equation (1), we have not accounted for any deviations from stoichiometry. It is well established[18-22] that the ion sputtering / high-temperature vacuum-annealing preparation process causes rutile (110) samples to become slightly reduced, with the creation of a small but non-zero concentration point defects in the form of bridging oxygen vacancies on the surface and Ti interstitials in the bulk of the sample. The O vacancies are widely believed to significantly affect the surface chemistry of rutile (110) compared to stoichiometric surfaces due to the resultant under-coordinated surface Ti atoms at these vacancy sites. Such vacuum-annealed samples typically show O vacancy coverages of about 2 - 12% depending on the preparation conditions.[71] The exact physical process which causes the vacancies to appear during annealing is not known, although molecular desorption experiments combined with STM have been used to characterise these defects[72] and shed new light on their origin.[73] It is also well known that surface vacancies are healed by exposing the sample to O_2, although, depending on the temperature and partial O_2 pressure, this process is usually accompanied by further adsorption of O to surface 5*f*-Ti sites[74] and the appearance of additional O-based surface adstructures.[20,71,75-76] It is worth mentioning that there is one STM study which apparently shows a perfectly stoichiometric rutile (110) surface.[77] Despite the sensitive dependence of the surface structure on the preparation conditions, the fact that the surface vacancies are healed upon exposure to O_2 confirms that the stoichiometric surface is energetically favourable over O-reduced surfaces as one might reasonably expect.

Alongside surface O vacancies, the influence of bulk Ti interstitials on the appearance of the (110) surface must also be considered. Investigations into the behaviour of Ti interstitials and their implications for the surface chemistry of rutile are still ongoing,[65,78] and it is not yet entirely clear whether Ti interstitials located in the bulk of the material have any significant consequences for the energetic stability of step structures occurring on the surface. There is recent evidence which suggests that bulk Ti interstitials do not influence (110) terraces in a significant way: In a recent study by Bechstein et al.,[78] the Ti interstitial defect formation energy was calculated at (110) terrace sites and found to be 1.2 eV higher than the formation energy at bulk Ti interstitial sites. This suggests that for mostly flat (110) samples, like that shown in Figure 9 (b), Ti interstitials are likely to quickly diffuse away from the surface and into the bulk of the material. O vacancies are therefore likely to be the dominant form of point defects which contribute to the overall surface chemistry on (110) terraces with low step density. However, it is not completely clear as to whether Ti interstitials are repelled by steps in the same way as they are by (110) terraces. In Bechstein's article,[78] it was theoretically predicted that for rutile surfaces with a high step density, Ti interstitials are *more* stable at $\langle 1\bar{1}1\rangle_R$ step sites than they are at bulk sites by about 0.5 eV. This prediction was then used to argue in favour of a mechanism by which O-deficient strand structures extended along $\langle 001\rangle$ directions are formed during annealing on high-index surfaces, where Ti interstitials migrate to the surface to form the strands, with the $\langle 1\bar{1}1\rangle_R$ steps as their exit points. This was corroborated with STM data which showed a rutile (771) surface of high step density after annealing at about 900 K, where strand structures extended along $\langle 001\rangle$ directions were seen to be protruding from the steps. A mostly flat (110) surface was shown in the same article, in which only a tiny number of such strand structures were seen. The authors argued quite plausibly that more building material is available on surfaces with a high step density due to the larger proportion of undercoordinated surface atoms, which explains the propensity of highly-stepped surfaces to form such strands. In addition to this, we also speculate that the net diffusion tendencies of Ti interstitials from the surface may also be a question of the competition between the repulsive influence of (110) terraces and the attractive influence of steps, and therefore dependent on step density as well as temperature. With slowly decaying surface-surface interactions, gaining a fuller picture of the energetic landscape and migration pathway barriers for Ti interstitials is not likely to be a trivial task using a DFT approach. Full DFT calculations of Ti interstitial migration paths and preferred binding sites as a function of surface roughness would require supercells which are currently prohibitively large, especially for surfaces of low step density. Nevertheless, the good agreement of our stoichiometric theoretical models with experimentally observed slightly nonstoichiometric samples suggests that the O vacancies and Ti interstitials can be regarded as an artefact of the annealing process which otherwise have no effect on overall island shapes.

Secondly, on visual inspection, it appears that the left and right edges of the island are bevelled by $[1\bar{1}0]$-type steps, where the corresponding kinks are labelled 2, 4, 7 and 9 in a rudimentary sketch in Figure 9 (c). Another instance of an apparent $[1\bar{1}0]$-type structure is highlighted in the smaller of the two circled regions in Figure 9 (b). The apparent $[1\bar{1}0]$-like features seen on the island are tiny; no more than 2 bright Ti rows in extent, or 4 atoms. Because of the periodic boundary conditions used in our calculations, we effectively simulate steps which are infinitely long. This means that our calculations do not account for subtleties such as the free energy of kinks, their interactions among themselves and with steps, and the atomic structure of kinks. This therefore means that our step energies can only reliably be compared to steps which are of appreciable length in STM images, at least for the purposes of using Wulff constructions. It is therefore doubtful that an infinitely long $\langle 1\bar{1}0\rangle$-type step under periodic boundary conditions would be representative of the $[1\bar{1}0]$-like structure which is only 4 atoms wide, the atomic configuration and energy of which will be largely determined by the fact that at least 2 of these atoms must form bonds with the two adjoining steps. It is also worth pointing out that the island observed by Diebold et al.[20] did not exhibit these apparent $[1\bar{1}0]$-type steps. In any case, the $[1\bar{1}0]$-like features comprise a negligible proportion of the total population of steps across the whole image and so they were deemed too insignificant to warrant further investigation.

Thirdly, the island habit has an apparent chirality, in that the kinks labelled 3 and 8 (or equivalently, 2, 4, 7 and 9) are not located exactly opposite each other along the direction $[001]$. This chirality is also quite apparent in Diebold's image.[20] Our main comment on this is that the Wulff construction is a scheme for predicting the habit of crystals in the macroscopic regime, whereas the island is microscopic in size. It is known that the bright rows observed with STM correspond to the 5-fold coordinated Ti atoms and the dark rows are bridging O atoms[77] (see

Figure 1). With close inspection of the lower terrace from the STM image of Figure 9 (b), it can be verified that the island spans no more than about 15 such rows, and therefore 15 surface cells. Given that the island's entire extent is only one order of magnitude larger than the size of one of its irreducible surface cell component parts, and that we have made no account of the possible atomic arrangements at the kinks, it is entirely plausible that the experimentally observed island habit at such microscopic scales is subject to aliasing of this kind, resulting in kinks 3 and 8 being misaligned by one or two unit cells. It is also unsurprising due to initial small and random configurational perturbations almost certainly being present in the initial growth environment. Fourthly, no accounts of the energetic contributions of the kinks or step-step interactions were accounted for by the Wulff constructions.

4. CONCLUSIONS

We have presented a DFT/supercell methodology for calculating the terrace free energy per unit area, step free energy per unit length and step-step interaction energy of high-index vicinal surfaces of crystalline solids using slab models. The slow oscillatory convergence of the individual energetic components (terrace, step and step-step interactions) of vicinal surfaces with increasing slab dimensions due to QSE has been demonstrated for the case of TiO_2 rutile. For such systems in which QSE are strong, we have argued that using a statistical linear fit of total slab energy against increasing slab size is an unreliable and misleading approach to calculating surface energies, and therefore an unreliable way of evaluating the energies of steps. For this reason, we argue instead that step energies and step interaction energies should all be individually plotted against slab size and checked for consistency via a layer-by-layer cross-check of the low-index terrace surface energy, calculated separately using the appropriate low-index slabs. This method has been applied to two $\langle 1\bar{1}1 \rangle$-direction steps and two $\langle 001 \rangle$-direction steps on the rutile (110) surface using DFT with the GGA PBE functional, following published STM studies[18-22] which have repeatedly shown that step defects are extended solely along the directions $\langle 1\bar{1}1 \rangle$ and $\langle 001 \rangle$. The specific atomic arrangements of the steps studied were those recently predicted to be the most energetically stable overall by Martinez et al.[23] The two $\langle 001 \rangle$-direction steps, $\langle 001 \rangle_{Ti}$ and $\langle 001 \rangle_{O}$, were found to be very similar in energy and so it was concluded that these two structures are likely to occur on laboratory samples with approximately equal probability. The $\langle 1\bar{1}1 \rangle_{R}$ structure was found to be significantly more stable than the $\langle 1\bar{1}1 \rangle$ structure. 2D Wulff constructions were used with the theoretically calculated step energies to show that the shape of islands with $\langle 1\bar{1}1 \rangle_{R}$ steps compare well with STM data, whereas the shape of an island with $\langle 1\bar{1}1 \rangle$ steps does not stand up to experimental evidence.

ASSOCIATED CONTENT

Supporting Information.

Argument against linear fitting method of evaluating surface energy, elementary derivation of high-index surface energy equation and application to supercells, and discussion of statistical uncertainty of geometry-optimized slab energies. This material is available free of charge via the Internet at http://pubs.acs.org.

AUTHOR INFORMATION

Corresponding Author

*Andrew J. Scott; E-mail a.j.scott@leeds.ac.uk

Notes

The authors declare no competing financial interests.

ACKNOWLEDGMENTS

T. P. H. would like to thank the UK EPSRC for the Doctoral Training Award which funded this research. T. P. H. would also like to thank Stefan Wendt for helpful discussions. This work was undertaken using the high performance computing facilities ARC1 at The University of Leeds and the STFC Hartree Centre at the STFC Daresbury Laboratory. We acknowledge use of Hartree Centre resources in this work. The STFC Hartree Centre is a research collaboration in association with IBM providing High Performance Computing platforms funded by the UK's investment in e-Infrastructure. The Centre aims to develop and demonstrate next generation software, optimized to take advantage of the move towards exa-scale computing.

ABBREVIATIONS

QSE, quantum size effects; DFT, density functional theory; STM, scanning tunneling microscopy; MP, Marchenko and Parshin interaction potential; GGA PBE, generalized gradient approximation parameterized by Perdue, Burke and Ernzerhof; SCF, self-consistent field; LBFGS, low-memory Broyden-Fletcher-Goldfarb-Shanno optimization algorithm.

REFERENCES

[1]Fujishima A.; Rao T. N.; Tryk D. A. Titanium dioxide photocatalysis. *J Photoc. Photobio. C* **2000,** *1*, 1-21

[2]Huang Z.; Maness P.-C.; Blake D. M.; Wolfrum E. J.; Smolinski S. L.; Jacoby W. A. Bactericidal mode of titanium dioxide photocatalysis. *J Photoc. Photobio. A* **2000,** *130*, 163-170

[3]Maness P.; Smolinski S.; Blake D. M.; Huang Z.; Wolfrum E. J.; Jacoby W. A. Bactericidal Activity of Photocatalytic TiO_2 Reaction: toward an Understanding of Its Killing Mechanism. *Appl. Environ. Microbiol.* **1999**, *65*, 4094-4098

[4]Sunada K.; Kikuchi Y.; Hashimoto K.; Fujishima A. Bactericidal and Detoxification Effects of TiO_2 Thin Film Photocatalysts. *Environ. Sci.Technol.* **1998**, *32*, 726-728

[5]Ollis D. F.; Pelizzetti E.; Serpone N. Destruction of Water Contaminants. *Environ. Sci.Technol.* **1991,** *5*, 1522-1529

[6] Gaya U. I.; Abdullah A. H. Heterogeneous photocatalytic degradation of organic contaminants over titanium dioxide: A review of fundamentals, progress and problems. *J Photoc. Photobio. C* **2008**, *9*, 1-12

[7] Wang R.; Hashimoto K.; Fujishima A.; Chikuni M.; Kojima E.; Kitamura A.; Shimohigoshi M.; Watanabe T. Light-induced amphiphilic surfaces. *Nature* **1997,** *388*, 431-432

[8] Wang R.; Hashimoto K.; Fujishima A.; Chikuni M.; Kojima E.; Kitamura A.; Shimohigoshi M.; Watanabe T. Photogeneration of Highly Amphiphilic TiO_2 Surfaces. *Adv. Mater.* **1998**, *10*, 135-138

[9] Paz Y.; Luo Z.; Rabenberg L.; Heller A. Photooxidative self-cleaning transparent titanium dioxide films on glass. *J. Mater. Res.* **1995**, *10*, 2842-2848

[10] Livi K. J. T.; Schaffer B.; Azzolini D.; Seabourne C. R.; Hardcastle T. P.; Scott A. J.; Sverjensky D.; Hazen R. M.; Erlbacher J. D.; Brydson R. M. D. Atomic-scale surface roughness of rutile and implications for organic molecule adsorption. *Langmuir* **2013**, *29*, 6876-6883

[11] Machesky M. L.; Wesolowski D. J.; Palmer D. A.; Ridley M. K. On the Temperature Dependence of Intrinsic Surface Protonation Equilibrium Constants: An Extension of the Revised MUSIC Model. *J. Colloid Interf. Sci.* **2001**, *239*, 314-327

[12] Ridley M. K.; Machesky M. L.; Wesolowski D. J.; Palmer D. A. Modeling the surface complexation of calcium at the rutile-water interface to 250°C. *Geochim. Cosmochim. Ac.* **2004**, *68*, 239-251

[13] Cleaves H. J. II; Scott A. M.; Hill F. C.; Leszczynski J.; Sahai N.; Hazen R. Mineral-organic interfacial processes: potential roles in the origins of life. *Chem. Soc. Rev*. **2012**, *41*, 5502-5525

[14] Bahri S.; Jonsson C. M.; Jonsson C. L.; Azzolini D.; Sverjensky D.; Hazen R. M. Adsorption and Surface Complexation Study of L-DOPA on Rutile (r-TiO2) in NaCl Solutions. *Environ. Sci. Technol.* **2011**, *45*, 3959-3966

[15] Machesky M.; Wesolowski D.; Rosenqvist J.; Předota M.; Vlcek L.; Ridley M.; Kohli V.; Zhang Z.; Fenter P.; Cummings P. et al. Comparison of Cation Adsorption by Isostructural Rutile and Cassiterite. *Langmuir* **2011**, *27*, 4585-4593

[16] Diebold U. The Surface Science of Titanium Dioxide. *Surf. Sci. Rep.* **2003**, *48*, 53-229

[17] Ramamoorthy M.; Vanderbilt D.; King-Smith R. D. First-principles calculations of the energetics of stoichiometric TiO_2 surfaces. *Phys. Rev. B* **1994**, *49*, 16721-16727

[18] Onishi H.; Iwasawa Y. STM-imaging of formate intermediates adsorbed on a TiO_2 (110) surface. *Chem. Phys. Lett.* **1994**, *226*, 111-114

[19] Onishi H.; Fukui K.; Iwasawa Y. Atomic-Scale Surface Structures of TiO_2 (110) Determined by Scanning Tunneling Microscopy: A New Surface-Limited Phase of Titanium Oxide. *B. Chem. Soc. Jpn.* **1995**, *68*, 2447-2458

[20] Diebold U.; Lehman J.; Mahmoud T.; Kuhn M.; Leonardelli G.; Hebenstreit W.; Schmid M.; Varga P. Intrinsic defects on a TiO_2 (110) (1×1) surface and their reaction with oxygen: a scanning tunneling microscopy study. *Surf. Sci.* **1998**, *411*, 137-153

[21] Martinez U.; Hansen J. Ø.; Lira E.; Kristoffersen H. H.; Huo P.; Bechstein R.; Lægsgaard E.; Besenbacher F.; Hammer B.; Wendt S. Reduced Step Edges on Rutile TiO_2 (110) as Competing Defects to Oxygen Vacancies on the Terraces and Reactive Sites for Ethanol Dissociation. *Phys. Rev. Lett.* **2012**, *109*, 155501

[22] Li M.; Hebenstreit W.; Gross L.; Diebold U.; Henderson M. A.; Jennison D. R.; Schultz P. A.; Sears M. P. Oxygen-induced restructuring of the TiO_2 (110) surface: a comprehensive study. *Surf. Sci.* **1999,** *437***,** 173-190

[23] Martinez U.; Vilhelmsen L. B.; Kristoffersen H. H.; Stausholm-Møller J.; Hammer B. Steps on Rutile TiO_2(110): Active Sites for Water and Methanol Dissociation. *Phys. Rev. B* **2011**, *84*, 205434

[24] Wu X.; Selloni A.; Nayak S. K. First principles study of CO oxidation on TiO_2(110): The role of surface oxygen vacancies. *J. Chem. Phys.* **2004**, *120,* 4512-4516

[25] Thompson S. J.; Lewis S. P. Revisiting the (110) surface structure of TiO_2: A theoretical analysis. *Phys. Rev. B* **2006**, *73*, 073403

[26] Hameeuw K. J.; Cantele G.; Ninno D.; Trani F.; Iadonisi G. The rutile TiO_2 (110) surface: Obtaining converged structural properties from first-principles calculations. *J. Chem. Phys.* **2006**, *124*, 024708

[27] Bates S. P.; Kresse G.; Gillan M. J. A systematic study of the surface energetics and structure of TiO_2(110) by first-principles calculations. *Surf. Sci.* **1997**, *385*, 386-394

[28] Rasmussen M. D.; Molina L. M.; Hammer B. Adsorption, diffusion, and dissociation of molecular oxygen at defected TiO_2(110): A density functional theory study. *J. Chem. Phys.* **2004**, *120*, 988-997

[29] Oviedo J.; San Miguel M. A.; Sanz J. F.; Oxygen vacancies on TiO_2 (110) from first principles calculations. *J. Chem. Phys*. **2004**, *121*, 7427-7433

[30] Zhang C.; Lindan P. J. D. Multilayer water adsorption on rutile TiO_2 (110): A first-principles study. *J. Chem. Phys.* **2003**, *118*, 4620-4630

[31] Lindan P. J. D.; Zhang C. Exothermic water dissociation on the rutile TiO_2 (110) surface. *Phys. Rev. B* **2005**, *72*, 075439

[32] Harris L. A.; Quong A. A. Molecular Chemisorption as the Theoretically Preferred Pathway for Water Adsorption on Ideal Rutile TiO_2 (110). *Phys. Rev. Lett.* **2004**, *93*, 086105

[33] Perron H.; Vandenborre J.; Domain C.; Drot R.; Roques J.; Simoni E.; Ehrhardt J.-J.; Catalette H. Combined investigation of water sorption on TiO_2 rutile (110) single crystal face: XPS vs. periodic DFT *Surf. Sci.* **2007**, *601*, 518-527

[34] Bredow T.; Giordano L.; Cinquini F.; Pacchioni G. Electronic properties of rutile TiO_2 ultrathin films: Odd-even oscillations with the number of layers. *Phys. Rev. B* **2004**, *70*, 035419

[35] Kiejna A.; Pabisiak T.;; Gao S.W. The energetics and structure of rutile TiO_2 (110) *J. Phys-Cond. Mat.* **2006**, *18*, 4207-4217

[36] Perron H.; Domain C.; Roques J.; Drot R.; Simoni E.; Catalette H. Optimisation of Accurate Rutile TiO_2 (110), (100), (101) and (001) Surface Models from Periodic DFT Calculations. *Theor. Chem. Acc.* **2007**, *117*, 565-574

[37] Hardcastle T. P.; Brydson R.M.D.; Livi K.J.T.; Seabourne C.R.; Scott A.J. Ab-initio modelling, polarity and energetics of clean rutile surfaces in vacuum and comparison with water environment. *J. Phys. Conf. Ser.* **2012**, *371*, 012059

[38] Boettger J. C. Persistent quantum-size effect in aluminum films up to twelve atoms thick. *Phys. Rev. B* **1996**, *53*, 13133

[39]Gay J. G.; Smith J. R.; Richter R.; Arlinghaus F. J.; Wagoner R. H. Summary Abstract: Surface energies in d-band metals. *J. Vac. Sci. Technol. A* **1984**, *2*, 93-94

[40]Gong X.-Q.; Selloni A.; Batzill M.; Diebold U. Steps on anatase TiO_2 (101). *Nat. Mater.* **2006**, *5*, 665-670

[41]Koslov S. M.; Vin F.; Nilius N.; Shaikhutdinov S.; Neyman K. M. Absolute Surface Step Energies: Accurate Theoretical Methods Applied to Ceria Nanoislands. *J. Phys. Chem. Lett.* **2012**, *3*, 1956-1961

[42]Li B.; Michaelides A.; Scheffler M. Density functional theory study of flat and stepped NaCl(001). *Phys. Rev. B* **2007**, *76*, 075401

[43]Yu B. D.; Scheffler M. Ab initio study of step formation and self-diffusion on Ag (100). *Phys. Rev. B* **1997,** *55*, 13916-13924

[44]Frenken J. W. M.; Stoltze P. Are Vicinal Metal Surfaces Stable? *Phys. Rev. Lett.* **1999**, *82*, 3500-3503

[45]Barreteau C.; Raouafi F.; Desjonquères M.C.; Spanjaard D. Modelling of transition and noblemetal vicinal surfaces: energetics, vibrations and stability. *J. Phys-Cond. Mat.* **2003**, *15*, S3171–S3196

[46]Raouaf F.; Barreteau C.; Raouafi F.; Desjonquères M.C.; Spanjaard D. Energetics of stepped and kinked surfaces of Rh, Pd and Cu from electronic structure calculations. *Surf. Sci.* **2002**, *505*, 183-199

[47]Williams E. D. Surface steps and surface morphology: understanding macroscopic phenomena from atomic observations. *Surf. Sci.* **1994**, *299*, 502-524

[48] Gruber E. E.; Mullins W. W. On the theory of anisotropy of crystalline surface tension. *J. Phys. Chem.* Solids **1967**, *28*, 875-887

[49] Jayaprakash C.; Rottman C.; Saam W. F. Simple model for crystal shapes: Step-step interactions and facet edges. *Phys. Rev. B* **1984**, *39*, 6549-6554

[50] Marchenko V. I.; Parshin A. Y. Elastic properties of crystal surfaces. *Zh. Eksp. Teor. Fiz+* **1981**, *79*, 257-260

[51] Barbier L.; Masson L.; Cousty J.; Salanon B. Roughening of vicinal surfaces and step-step interactions: application to Cu(1,1,11) by means of statistical analysis of STM images. *Surf. Sci.* **1996**, *345*, 197-212

[52] Masson L.; Barbier L.; Cousty J.; Salanon B. Statistical analysis of STM images and measurement of the step-step interaction on Cu vicinaf surfaces. *Surf. Sci.* **1994**, *317*, L1115-L1119

[53] García N.; Serena P. A. Quantum effects on the step interaction energy and the equilibrium shape of crystals. *Surf. Sci.* **1995**, *330*, L665-L667

[54] Nowicki M.; Bombis C.; Emundts A.; Bonzel H. P.; Wynblatt P. Step–step interactions and universal exponents studied via three-dimensional equilibrium crystal shapes. *New J. Phys.***2002**, *4*, 60.1-60.7

[55] Najafabadi R.; Srolovitz D. J. Elastic step interactions on vicinal surfaces of fee metals. *Surf. Sci.* **1994**, *317*, 221-234

[56] Redfield A. C.; Zangwill A. Attractive interactions between steps. *Phys. Rev. B* **1992**, *46,* 4289-4291

[57]Kukta R. V.; Peralta A.; Kouris D. Elastic Interaction of Surface Steps: Effect of Atomic-Scale Roughness. *Phys. Rev. Lett.* **2002**, *88*, 186102

[58]Swamy K.; Bertel E.; Vilfan I. Step interaction and relaxation at steps: Pt(110). *Surf. Sci.* **1999**, *425*, L369-L375

[59]van Dijken S.; Zandvliet H. J. W.; Poelsema B. Anomalous strong repulsive step-step interaction on slightly misoriented Si(113). *Phys. Rev. B* **1997**, *55*, 7864-7867

[60]Frohn J.; Giesen M.; Poensgen M.; Wolf J. F.; Ibach H. Attractive Interaction between Steps. *Phys. Rev. Lett.* **1991**, *67*, 3543-3547

[61]Clark S. J.; Segall M. D.; Pickard C. J.; Hasnip P. J.; Probert M. J.; Refson K.; Payne M. C. First principles methods using CASTEP. *Z. Kristallogr.* **2005**, *220*, 567-570

[62]Perdew J. P.; Burke K.; Ernzerhof M. Generalized gradient approximation made simple. *Phys. Rev. Lett.* **1996**, *77*, 3865-3868

[63]Vanderbilt D. Soft self-consistent pseudopotentials in a generalized eigenvalue formalism. *Phys. Rev. B* **1990**, *41*, 7892-7895

[64]Li M.; Hebenstreit W.; Diebold U. Oxygen-induced restructuring of the rutile TiO_2 (110) (1×1) surface. *Surf. Sci.* **1998**, *414*, L951-L956

[65]Liu D. C.; Nocedal J. On the limited memory BFGS method for large scale optimization. *Math. Program.* **1989**, *45*, 503-528

[66]Broyden C. G. The Convergence of a Class of Double-rank Minimization Algorithms

1. General Considerations. *IMA J. Appl. Math.* **1970**, *6*, 76-90

[67]Broyden C. G. The Convergence of a Class of Double-rank Minimization Algorithms 2. The New Algorithm. *IMA J. Appl. Math.* **1970**, *6*, 222-231

[68]Fletcher R. A new approach to variable metric algorithms. *Comput. J.* **1970**, *13*, 317-322

[69]Goldfarb D. A family of variable-metric methods derived by variational means. *Math. Comput.* **1970**, *24*, 23-26

[70]Shanno D. F. Conditioning of quasi-Newton methods for function minimization. *Math. Comput.* **1970**, *24*, 647-656

[71]Lira E.; Huo P.; Hansen J.Ø.; Rieboldt F.; Bechstein R.; Wei Y.; Streber R.; Porsgaard S.; Li Z.; Lægsgaard E. et al. Effects of the crystal reduction state on the interaction of oxygen with rutile TiO_2(110). *Catal. Today* **2012**, *182*, 25-38

[72]Lira E.; Wendt S.; Huo P.; Hansen J. Ø.; Streber R.; Porsgaard S.; Wei Y.; Bechstein R.; Lægsgaard E.; Besenbacher F. The Importance of Bulk Ti^{3+} Defects in the Oxygen Chemistry on Titania Surfaces. *J. Am. Chem. Soc.* **2011**, *133*, 6529-6532

[73]Wendt S.; Schaub R.; Matthiesen J.; Vestergaard E. K.; Wahlström E.; Rasmussen M. D.; Thostrup P.; Molina L. M.; Lægsgaard E.; Stensgaard I. et al. Oxygen vacancies on TiO_2(110) and their interaction with H_2O and O_2: A combined high-resolution STM and DFT study. *Surf. Sci.* **2005**, *598*, 226-245

[74]Du Y.; Dohnálek Z.; Lyubinetsky I. Transient Mobility of Oxygen Adatoms upon O_2 Dissociation on Reduced TiO_2(110). *J. Phys. Chem. C* **2008**, *112*, 2649-2653

[75]Wang L.-Q.; Baer D.R.; Engelhard M.H. Creation of variable concentrations of defects on TiO_2(110) using low-density electron beams. *Surf. Sci.* **1994**, *320*, 295-306

[76] Pan J.-M.; Maschhoff B. L.; Diebold U.; Madey T. E. Interaction of water, oxygen, and hydrogen with TiO_2(110) surfaces having different defect densities. *J. Vac. Sci. Tech. A* **1992**, *10*, 2470-2476

[77] Diebold U.; Anderson J. F.; Ng K.-O.; Vanderbilt D. Evidence for the Tunneling Site on Transition-Metal Oxides: TiO_2(110). *Phys. Rev. Lett.* **1996**, *77*, 1322-1325

[78] Bechstein R.; Kristoffersen H. H.; Vilhelmsen L. B.; Rieboldt F.; Stausholm-Møller J.; Wendt S.; Hammer B.;; Besenbacher F. Packing Defects into Ordered Structures: Strands on TiO_2. *Phys. Rev. Lett.* **2012**, *108*, 236103

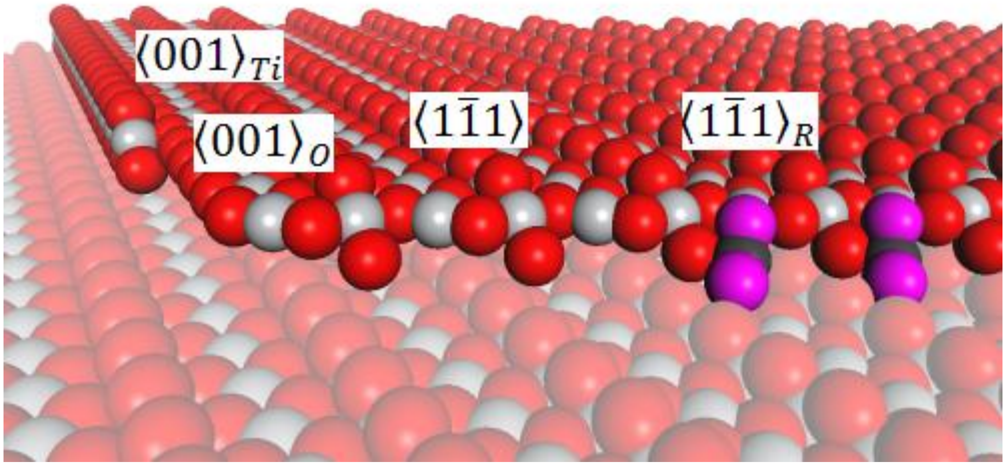
$\langle 001\rangle_{Ti}$
$\langle 001\rangle_{O}$
$\langle 1\bar{1}1\rangle$
$\langle 1\bar{1}1\rangle_{R}$

T.O.C. image